

Characterization of laser ablation of solid targets with near-infrared laser pulses of 100 fs and 1 ps duration

S. Amoruso^{a,*}, G. Ausanio^b, R. Bruzzese^a, L. Gragnaniello^a,
L. Lanotte^b, M. Vitiello^a, X. Wang^a

^a *Coherentia CNR-INFN and Dipartimento di Scienze Fisiche, Università degli Studi di Napoli “Federico II”,
Complesso Universitario di Monte S. Angelo, Via Cintia, I-80126 Napoli, Italy*

^b *Coherentia CNR-INFN and Dipartimento di Scienze Fisiche, Università degli Studi di Napoli “Federico II”,
Piazzale Tecchio 80, I-80125 Napoli, Italy*

Received 3 May 2005; accepted 23 June 2005

Available online 24 October 2005

Abstract

The process of laser ablation of silicon targets with ≈ 1 ps/1055 nm and ≈ 100 fs/780 nm laser pulses has been investigated by exploiting optical emission spectroscopy and fast photography of the ablated species in the gas phase, and atomic force microscopy of less than one layer deposits of the ablated material. We have observed, for both durations, the presence of a fast atomic component followed by a much slower plume of nanoparticles of the target material. For both laser pulses, experimental ablation thresholds have been compared with the prediction of a simple theoretical model, resulting in pretty good agreement. The properties of size distribution of the silicon nanoparticles have been analyzed as a function of the laser pulse intensity, and also compared with the results for metallic targets. Our experimental results show that the generation of nanoparticles, with pretty narrow size distributions, is a characteristic feature of the interaction of ultrashort laser pulses with solids (namely, metals and semiconductors), for both ≈ 1 ps and ≈ 100 fs laser pulse durations.

© 2005 Elsevier B.V. All rights reserved.

PACS: 79.20Ds; 52.38Mf; 52.50Jm; 52.50Lp

Keywords: Ultrashort laser ablation; Nanoparticles; Spectroscopy; Fast imaging

1. Introduction

The interaction of ultrashort laser pulses with materials is currently receiving a great interest in virtue of its peculiar applications, and also thanks to the availability of more reliable laser systems. High intensity, ultrashort laser pulses can significantly reduce the extent of heat conduction into the target, leading the irradiated material in extreme conditions of temperature and pressure, while remaining at almost solid density [1,2]. The subsequent relaxation of the heated material results in the ablation of the target surface with expulsion of matter in the form of atoms and ions, as well as clusters and nanoparticles. Ultrashort laser ablation is useful in several applications

concerning laser modification of surfaces (e.g. drilling, cutting, patterning), or film growth by pulsed laser deposition (PLD) [3,4].

Notwithstanding the ever-increasing use of ultrashort laser pulses in laser ablation and related applications, a thorough knowledge of the physical mechanisms of material removal, as well as of their dependence on laser characteristics and material properties, is still far from being complete [5]. Several experimental and theoretical studies of ultrashort laser ablation have been devoted to the analysis of modifications induced on the irradiated surface, mainly for micromachining purposes. In particular, the ablation rate as a function of the laser fluence has been extensively investigated [6–9]. Moreover, almost all the analyses have been performed in the case of Ti:sapphire laser pulses at a typical pulse duration of ≈ 100 fs. Instead, less work has been dedicated to the characterization of the material blow-off through the analysis of the generated plasma plume, as well as to the variation of its features with the laser pulse duration.

* Corresponding author.

E-mail address: amoruso@na.infn.it (S. Amoruso).

In this context, the aim of the present experimental work is to study the plasma plume produced by irradiating solid targets with both ≈ 1 ps and ≈ 100 fs laser pulses. In particular, we have used a Nd:glass laser system emitting ≈ 0.9 ps pulses at 1055 nm to investigate laser ablation of different materials, and compared the results with our previous findings obtained by using ≈ 100 fs, Ti:sapphire laser pulses [10–12]. We are thus in the condition of comparing results of ultrashort laser ablation of solid targets with pulse duration varying by almost one order of magnitude, at infrared wavelengths. The comparison between the two temporal regimes allows investigating the effect of pulse duration and intensity on the properties of the ablation plasma plume. In particular, we deal with two major issues of the ablation process: (i) the plume expansion in a vacuum, studied by fast imaging and optical emission spectroscopy; (ii) the dimensional properties of the nanoparticles generated via ultrashort laser ablation, through atomic force microscopy (AFM) analysis of the deposits of the ablated material. The analysis has been mainly carried out on silicon, a case study material for both the basic physics of the process and the technological applications. Moreover, laser ablation with ≈ 1 ps pulses is particularly interesting in such a case, since it is comparable to the characteristic time for lattice heating of silicon [13]. Some results on metals (e.g. nickel and silver) will be also briefly discussed, namely in the context of nanoparticles emission characterization.

The paper is organized in six sections. The experimental setup is discussed in Section 2. Sections 3 and 4 are devoted to laser ablation of silicon, and contain the results of the plasma plume expansion in a vacuum and the analysis of the ablation thresholds, respectively. Section 5 reports the characterization of the size distributions of the nanoparticles produced during laser ablation of silicon and metallic targets. Finally, the summary and conclusions are given in Section 6.

2. Experiment

The experimental setup is very similar to the one used in previous works on laser ablation with a Ti:sapphire, ≈ 100 fs laser [10–12], and will be briefly described here. Ablation experiments have been carried out by using a chirped pulse amplification (CPA)-based Nd:glass laser system that produces pulses of 0.9 ps duration at 1055 nm, with a maximum energy per pulse of ≈ 4 mJ, at a repetition rate of 33 Hz. The temporal profile of the pulses was monitored by a single shot background free autocorrelation technique. The laser radiation was focused to spot sizes of $\approx 1 \times 10^{-3}$ cm² on the samples surface, at an incident angle of 45°, and in p-polarization. The laser pulse energy was varied by means of calibrated attenuating plates. The targets were mounted on a rotating holder to minimize pit formation, and placed in a vacuum chamber evacuated to a residual pressure of $\leq 10^{-5}$ Pa. Viewing ports allowed optical emission accompanying the ablation plume to be monitored along axes parallel (x) and perpendicular (z) to the target surface.

Vacuum plume expansion has been investigated by acquiring single shot images of the plume emission, in the x - z plane, with an intensified charge coupled device camera

(ICCD) operating in time-gated detection mode (3 ns minimum temporal resolution). Each image was acquired by recording the plume total emission onto the ICCD, equipped with a 1024×1024 array, with a 3:1 magnification. To reduce the noise, a $2 \times$ binning was operated during image acquisition obtaining a spatial resolution of ≈ 100 μ m. The ICCD gain and gate width were adjusted for each image in order to compensate the reduction of the plume intensity during plume expansion. We have also obtained spectrally resolved measurements of the emitted light by imaging a slice of the plasma onto the entrance slit of a 0.25-m monochromator coupled to an ICCD camera, with an overall spectral resolution of ≈ 0.4 nm.

The size of the produced nanoparticles has been characterized by depositing the produced plume onto freshly cleaved mica substrates located about 30 mm away and held at room temperature. The deposited samples were analyzed with an AFM equipped with a sharpened silicon tip with a radius of less than 5 nm. The number of laser pulses used for deposition was carefully selected to obtain deposits of less than one layer in order to limit the influence of particles coalescence on the substrate. Thus, the observed nanoparticles size distributions can be safely assumed to reflect the actual size distribution of the free nanoparticles expanding in a vacuum and reaching the substrate.

3. Analysis of the silicon plasma plume in a vacuum

Figs. 1 and 2 show the images of the laser-induced plume emission produced during ablation of silicon with 0.9 ps/1055 nm laser pulses, in high vacuum. The images of Fig. 1 refer to short time delays τ_D (< 0.1 μ s) after the laser pulse hits the target, while Fig. 2 shows plume emission recorded after several microsecond time delays. To facilitate the identification of the various plume components, profiles of the emission intensity versus distance, obtained by integrating the emission along an axis parallel to the target surface, have been also reported on the left-hand side of each image. The images, which are fairly symmetric with respect to the normal to the target surface, allow the identification of various populations characterized by different expansion dynamics and temporal evolution of the emission intensity. At very short time delays ($\tau_D = 25$ ns, see Fig. 1(a)), we observe a three component structure of the plume emission: (i) a very fast population characterized by a faint emission, which extends from few to several millimeters from the target surface; (ii) a more intense, second population whose maximum emission is located at a distance of ≈ 1 mm; (iii) a third, slow component situated very close to the target surface, and whose expansion occurs on a microsecond timescale (see Fig. 2). At later times, the two fast components move away from the target surface and their emission strongly decreases, while the slower component still occupies a region very close to the target surface, as shown in Fig. 1(b). The full expansion of the slow plume component only occurs after very long time delays, as can be observed in the images of Fig. 2.

From the analysis of the plume images of Fig. 1 we observe that: (i) the most of the species belonging to the very fast population reach distances of tens of millimeters from the

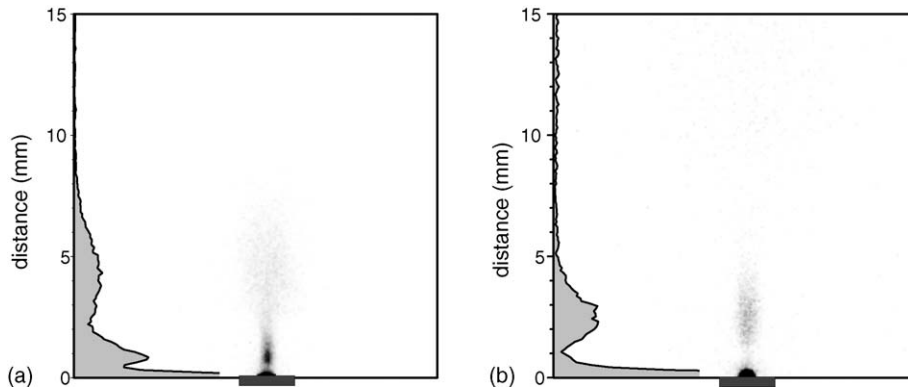


Fig. 1. Images of the plume expansion of a silicon plume produced by a 0.9 ps/1055 nm laser pulse at a fluence $F_L = 0.75 \text{ J/cm}^2$ ($I_L = 8.3 \times 10^{11} \text{ W/cm}^2$): (a) $\tau_D = (25 \pm 5) \text{ ns}$; (b) $\tau_D = (85 \pm 5) \text{ ns}$. Each image was recorded using a nominal 10 ns time gate on the intensifier of the camera. Distance 0 mm defines the front face of the target, which is shown as a grey box. The profile on the left-hand part of the image show the intensity vs. distance plot obtained by integrating the emission along a direction parallel to the target surface.

surface after less than 100 ns delay, indicating expansion velocities of the order of 10^7 cm/s , while their emission peak decreases by a factor of ≈ 10 ; (ii) the emission peak of the second fast component moves from ≈ 0.8 to $\approx 2.8 \text{ mm}$ in 60 ns, indicating an average expansion velocity of $\approx 3 \times 10^6 \text{ cm/s}$, while its intensity decreases by almost a factor 4. Moreover, both populations are characterized by a very forward peaked expansion. On the contrary, the slow population is characterized by a much larger angular divergence. Its front expands at a velocity of $\approx 10^5 \text{ cm/s}$, while the average velocity of the slow species is of the order of $\approx 10^4 \text{ cm/s}$. Moreover, emission from this component rests close to the target till very long time delays after the laser pulse, indicating a quite different velocity distribution of the slow component with respect to the more energetic part of the plume.

Spectrally resolved emission analysis of the laser produced plume revealed that the luminescence from the fast components is dominated by emission lines of the atoms of the target material, meanwhile the slow, delayed plume population emits a structureless broadband continuum spectrum. Thus, similarly to what we have already observed for laser ablation with $\approx 100 \text{ fs}$ Ti:sapphire laser pulses [10,11], we can ascertain that

the fast components are mainly formed by atoms and ions of the target material, while the slow component contains essentially nanoparticles with an average radius of the order of 10 nm (see Section 5).

In Fig. 3 we compare the velocity distributions of the ejected species obtained with the two laser pulses at an intensity of three to four times the ablation threshold (see Section 4). Fig. 3(a) shows the velocity distributions of the fast and slow components observed in the time-resolved images of the silicon plasma plume produced by a 0.9 ps/1055 nm pulse, at a laser intensity $I_L = 8.3 \times 10^{11} \text{ W/cm}^2$. Instead, Fig. 3(b) reports the velocity distributions of the different species ejected during 0.1 ps/780 nm laser ablation of silicon at a laser intensity $I_L = 5.0 \times 10^{12} \text{ W/cm}^2$, obtained by time-resolved spectral measurements of the laser-induced plasma plume emission [10,12].

For both laser pulses, we observe: (i) a first, high velocity population with an average velocity of the order of $(\approx 1-2) \times 10^7 \text{ cm/s}$, which is mainly composed of silicon ions; (ii) a second, fast population with an average velocity of $(\approx 2-3) \times 10^6 \text{ cm/s}$, which contains both neutral and ionized silicon atoms; (iii) a population of very slow particles with velocities

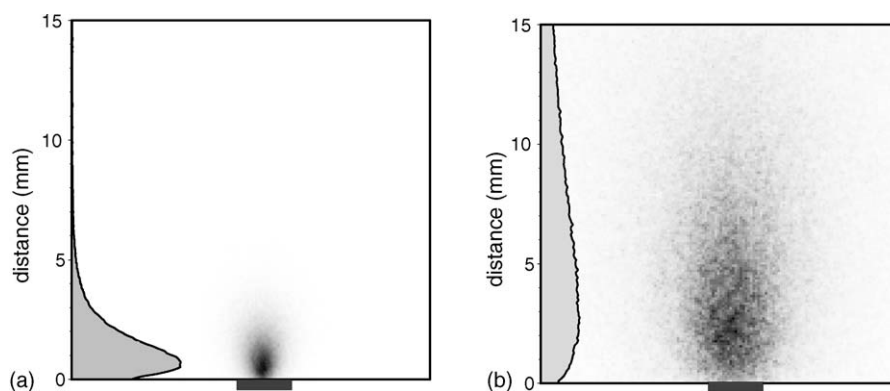


Fig. 2. Images of the plume expansion of a silicon plume produced by a 0.9 ps/1055 nm laser pulse at a fluence $F_L = 0.75 \text{ J/cm}^2$ ($I_L = 8.3 \times 10^{11} \text{ W/cm}^2$): (a) $\tau_D = (5.5 \pm 0.5) \mu\text{s}$; (b) $\tau_D = (42.5 \pm 2.5) \mu\text{s}$. Images (a) and (b) were recorded using a time gate width of 1 and 5 μs , respectively, on the intensifier of the camera. Distance 0 mm defines the front face of the target, which is shown as a grey box. The profile on the left-hand part of the image show the intensity vs. distance plot obtained by integrating the emission along a direction parallel to the target surface.

below 10^5 cm/s, and characterized by a quite large velocity distribution. This last population is formed by silicon nanoparticles characterized by a blackbody-like emission with a temperature of ≈ 2000 K close to the target, which subsequently cool down during their vacuum expansion [14]. Therefore, for both laser pulses the laser-induced plume is characterized by a very similar structure.

The presence of high-energy ion peak during ultrashort laser ablation has been observed by various authors, and for different materials [15–18]. In particular, for experimental conditions comparable to those used in our studies, Ye and Grigoropoulos observed two components when analyzing the ion velocity distribution during 80 fs/780 nm laser ablation of Si by time-of-flight mass spectrometry [17]. These two components were mainly formed by single-ionized silicon atoms with average velocities of $\approx 10^7$ and $\approx 10^6$ cm/s, respectively, in good agreement with our findings. Actually, the very fast ion component constitutes a small fraction of the atomic plume, whose origin is still under discussion. Coulomb explosion has been proposed as a possible mechanism for the generation of these high-energy ions. In Coulomb explosion, energetic electrons overcoming the work function of the material escape from the target surface. Consequently, the strong electric field created by the charge separation between escaping electrons and parent ions pulls ions out of the laser impact area [19]. The

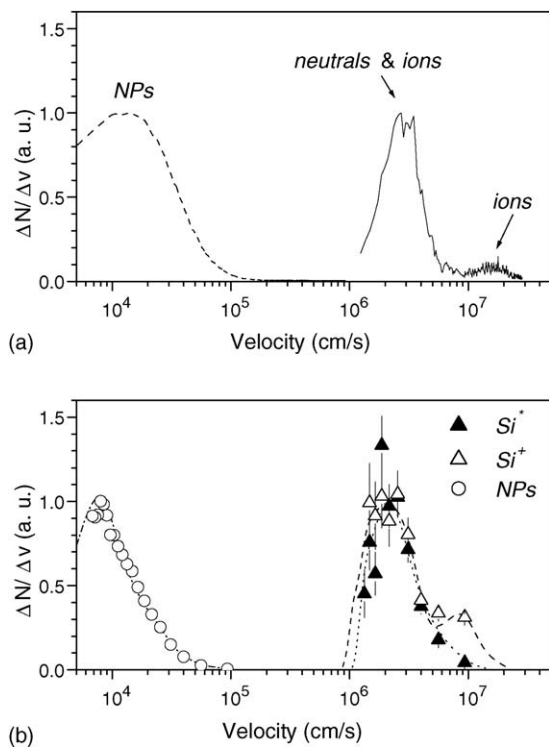


Fig. 3. (a) Velocity distributions of the ejected species obtained from the time-resolved images of the silicon plasma plume produced by a 0.9 ps/1055 nm pulse, at a laser fluence $F_L = 0.75$ J/cm 2 ($I_L = 8.3 \times 10^{11}$ W/cm 2); (b) velocity distributions of different species ejected during 0.1 ps/780 nm laser ablation of silicon obtained by time-resolved spectral measurements of the laser-induced plasma plume emission, at a laser fluence $F_L = 0.5$ J/cm 2 ($I_L = 5.0 \times 10^{12}$ W/cm 2): excited neutrals (Si^0), excited ions (Si^+) and nanoparticles (NPs). The velocity distribution profiles of the fast and slow part of the plume have been normalized to facilitate the comparison.

generation of high kinetic energy ions by surface Coulomb explosion has been demonstrated for dielectrics [20], while for semiconductors and metals the effectiveness of such a mechanism remains still controversial [21–25]. However, it is also likely that the energetic ions in the plume are produced through other space charge effects, like ambipolar diffusion e.g. [26,27].

4. Analysis of ablation thresholds of silicon

Laser ablation of solid targets exhibits a threshold behaviour: ablation occurs only when the laser intensity is higher than a certain value, which depends on both wavelength and duration of the laser pulse, as well as on the properties of the irradiated material. The ablation threshold can be determined by different methods, as for example visual inspection of the sample [28], crater depth measurements [7] and plasma radiation monitoring, which is considered to be proportional to the amount of ablated material [29,30]. The dependence of the ablation threshold on pulse duration and wavelength has been used as a useful approach to determine the mechanisms involved in laser light absorption in the material and its following relaxation and ablation [25,28,30].

In the present experiment we used plasma radiation monitoring to follow the dependence of the optical emission yield on the laser intensity, as shown in Fig. 4. In particular, we measured the overall optical emission signal from the different plasma plume species by integrating over the whole temporal interval for which an emission signal was detected. The ablation threshold intensities for the two laser pulses used in the present experiment have been obtained by extrapolating the emission yield to zero value, and result of $\approx 2 \times 10^{11}$ W/cm 2 (≈ 0.18 J/cm 2) for 0.9 ps/1055 nm and $\approx 1.5 \times 10^{12}$ W/cm 2 (0.15 J/cm 2) for 0.1 ps/780 nm laser pulses. These values are in pretty good agreement with those reported by Pronko et al. during laser irradiation of silicon targets at almost the same wavelengths and pulse durations [30].

In silicon, laser absorption can occur through different mechanisms, such as linear or multiphoton inter-band transi-

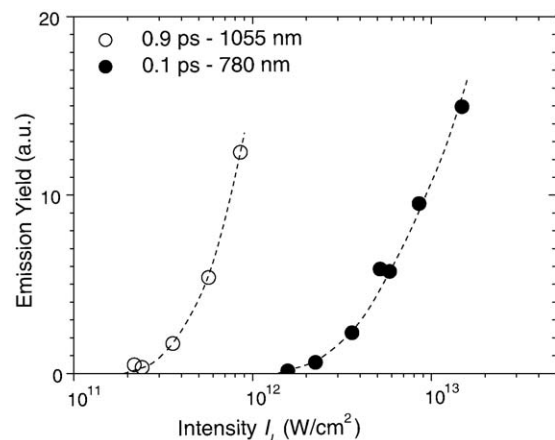


Fig. 4. Emission yield as a function of the laser intensity for 0.9 ps/1055 nm (○) and 0.1 ps/780 nm (●) laser pulses.

tions and avalanche ionization, depending on the laser fluence and wavelength [30,31]. For instance, in the visible Reitze et al. observed that two-photon absorption (TPA) dominates for laser fluences smaller than $\approx 0.1 \text{ J/cm}^2$, for 620 nm/90 fs laser pulses, while a stronger nonlinear absorption mechanism was active at larger fluences [31]. This has been ascribed to the onset of an avalanche ionization seeded by the electrons produced by TPA [30].

We present here an analytic estimate of the ablation threshold intensity and its scaling by assuming that avalanche ionization mechanisms are responsible for the absorption of laser light at the infrared wavelengths used in our study. Since in our experiments we are using silicon samples with an extrinsic resistivity of 10–50 $\Omega \text{ cm}$, representing an initial electron reservoir $N_{e,0}$ of $\approx 10^{14} \text{ electrons/cm}^3$, we neglected the effect of the TPA processes. The extrinsic electrons gain energy from the laser pulse electric field producing further ionization by collisions with the bound electrons when their energy overcomes the bandgap energy E_g (1.16 eV).

The temporal evolution of the electrons number density, $n_e(t)$, can be described by [28]:

$$\frac{dn_e}{dt} = \alpha I(t) n_e \quad (1)$$

where α is the avalanche coefficient. By considering a Gaussian pulse of duration τ_p (FWHM) with an intensity:

$$I(t) = I_0 \exp\left[-\frac{(4 \ln 2)t^2}{\tau_p^2}\right] \quad (2)$$

after integration we get

$$n_e(t) = n_{e,0} \exp\left[\sqrt{\frac{\pi}{4 \ln 2}} \alpha (1-R) I_0 \tau_p\right] \quad (3)$$

where R is the sample reflectivity.

Ablation occurs when the electron density reaches values high enough to induce a considerable absorption of the laser energy. In the modelling we choose the plasma critical density $n_{e,cr}$ as the theoretical indicator of macroscopic ablation. This choice is widely assumed in the literature [9,25–29], since it is just below this density that the laser radiation is strongly absorbed in a thin superficial layer. Nonetheless, Eq. (3) indicates that the dependence of the electron density on intensity is logarithmic: had we based our definition on a value of the electron density a factor 10 smaller, the threshold intensity would have decreased only by approximately 10%.

The threshold pulse peak intensity $I_{0,cr}$ of the Gaussian pulse, corresponding to the density $n_{e,cr}$ is then given by

$$I_{0,cr} = \frac{\sqrt{\frac{\pi}{4 \ln 2}}}{\alpha(1-R)\tau_p} \ln\left(\frac{n_{e,cr}}{n_{e,0}}\right) \quad (4)$$

while the corresponding intensity for a square pulse with a duration τ_p is given by

$$I_{sp,cr} = \sqrt{\frac{\pi}{4 \ln 2}} I_{0,cr} \approx 1.06 I_{0,cr} \quad (5)$$

The order of magnitude of the avalanche coefficient α has been estimated by considering the ionization coefficient provided by the Thornber dc semiempirical theory [32], scaled with the simplified expression for the ac electric response of Yablonoich and Bloembergen [33], and a collision frequency of the electrons with the atoms of the material of the order of 10^{15} s^{-1} [30,34]. For the laser intensity of concern here, the ionization coefficients result of the order of $(0.1-0.2) \times 10^{14} \text{ s}^{-1}$ at 0.9 ps/1055 nm and $(0.7-1.0) \times 10^{14} \text{ s}^{-1}$ at 0.1 ps/780 nm, and the corresponding avalanche coefficients are $\alpha \approx 0.1-0.2 \text{ cm}^2/\text{ps GW}$ and $\alpha \approx 0.1-0.15 \text{ cm}^2/\text{ps GW}$, respectively.

The threshold intensities obtained from Eqs. (4) and (5) are $(\approx 1-2) \times 10^{11} \text{ W/cm}^2$ at 0.9 ps/1055 nm, and $(\approx 0.15-2.1) \times 10^{12} \text{ W/cm}^2$ at 0.1 ps/780 nm, resulting in pretty good agreement with the experimental ones. The good agreement of the theoretical threshold values as well as the scaling with the wavelength is a good indication that the simple analytical model accounts for the most significant aspects of the laser absorption process at near-infrared wavelengths. For instance, Fig. 5 illustrates the evolution of the electron density produced by the 0.9 ps/1055 nm pulse at the laser peak intensity $I_{0,cr}$. We observe that the critical density plasma through electron avalanche is achieved late in the pulse. Thus, only the trailing edge of the pulse experiences strong absorption, or even reflection, for laser intensities larger than the ablation threshold.

In order to ascertain at which depth in the sample plasma formation occurs, we have estimated the penetration depth of the laser radiation for an intensity close to the ablation threshold. Pulse propagation into the material is governed by the balance equation:

$$\frac{\partial I(z,t)}{\partial z} = -\frac{\partial U_e}{\partial t} \approx \frac{U_e}{\tau_{av}} \quad (6)$$

where U_e is the energy per unit volume deposited into the sample and $\tau_{av} \approx (\alpha I_0)^{-1}$ is the time constant of energy deposition through avalanche ionization. By neglecting the transfer of energy to the lattice during the laser pulse, we have

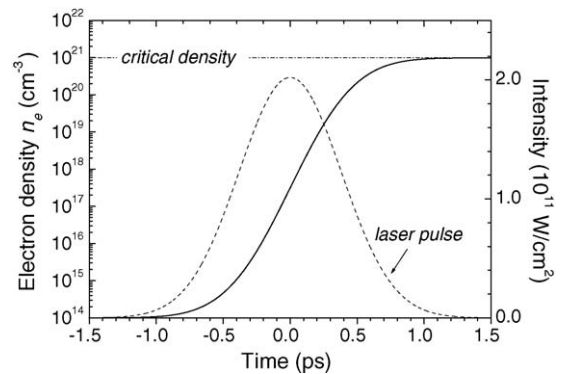


Fig. 5. Calculated free electron density for the irradiation of silicon with 0.9 ps/1055 nm laser pulse at the threshold intensity of $\approx 2 \times 10^{11} \text{ W/cm}^2$ (solid line). The dashed line shows the Gaussian laser pulse profile.

$U_e = n_e(E_g + \langle \epsilon_e \rangle) \approx n_e E_g$, $\langle \epsilon_e \rangle$ being the average electron energy. Then, we can estimate the absorption coefficient a as

$$a = -\frac{1}{I} \frac{\partial I}{\partial z} \approx \alpha n_e E_g \quad (7)$$

obtaining at the ablation threshold ($n_e \approx n_{e,cr}$) an absorption depth of $a^{-1} \approx 500$ nm and $a^{-1} \approx 200$ nm for 0.9 ps/1055 nm and 0.1 ps/780 nm, respectively. Therefore, at the ablation threshold a thin layer of dense plasma of the order of hundreds of nanometers is formed at the tail of the laser pulse. Above ablation threshold, the further absorption of laser energy can occur in an even thinner skin depth, and the laser pulse can be also partially reflected. Moreover, as the laser intensity increases, full ionization is achieved in the skin depth and the additional absorbed energy increases the average energy of the electrons. This energy is then transferred to the lattice on a picosecond timescale inducing ablation. Ablation can also occur through silicon lattice destabilization due to the weakening of the covalent bonding induced by the generation of a high concentration of excited electrons ($\approx 10^{22}$ electrons/cm³) [34,35].

5. Nanoparticles

We have obtained nanoparticles size-distributions in different irradiation conditions by depositing the produced plume onto mica substrates in vacuum, and at room temperature. The deposits have been analyzed through AFM. As an example, Fig. 6 shows the size distributions of the silicon nanoparticles, deposited with the two different laser pulses used in the present study: 0.9 ps/1055 nm (a), and 0.1 ps/780 nm (b), at laser intensities of approximately four times the ablation threshold. In both cases, we observe silicon nanoparticles with radii between few nm and ≈ 30 nm. The histogram of the nanoparticles radius r is fairly well described by a log-normal function:

$$f(r) = \frac{A_0}{\sqrt{2\pi}wr} \exp\left[-\frac{\ln\left(\frac{r}{r_c}\right)^2}{2w^2}\right] \quad (8)$$

where $f(r)$ is the frequency of nanoparticles with radius r , A_0 is a normalization constant and r_c and w are nanoparticles geometrical median radius and standard deviation of the logarithmic

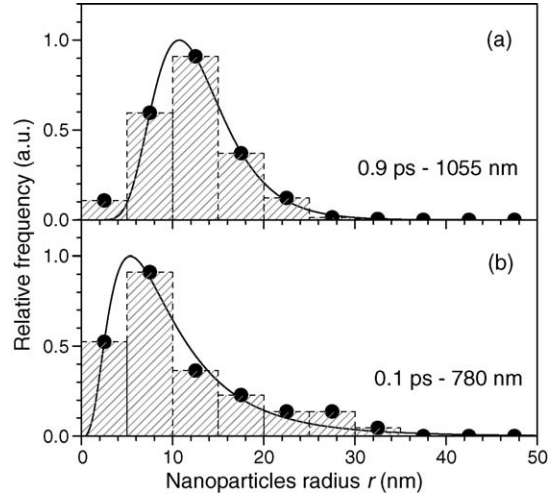


Fig. 6. Size distribution of the silicon nanoparticles produced during laser ablation with the two laser pulses at a laser intensities of the order of four times the ablation thresholds. The solid curve represents the fit to a log-normal distribution.

of the radius, respectively. The size statistics of the silicon nanoparticles are summarized in Table 1, in terms of median radius r_c , standard deviation of the logarithmic of the radius w , and most probable value of the radius, r_{peak} . We have also reported the radii r_- and r_+ below which 16 and 84% of the nanoparticles are counted (i.e. 68% of the NPs lie in between r_- and r_+). The observed size distributions show remarkable features which are pretty independent of laser pulse duration. In particular, we observe that the median radius r_c of the silicon nanoparticles is ≈ 5 –10 nm, while the peak radius, r_{peak} , generally does not exceed 10 nm for Si, in the investigated intensity range. The size distributions are fairly narrow, and $\approx 84\%$ of the nanoparticles show a radius below ≈ 20 nm, while both r_c and r_{peak} depend very slightly on the laser intensity at both pulse lengths. This suggests that also the properties characterizing the nanoparticles produced during ultrafast ablation with infrared laser pulses in the range 0.1–1 ps are pretty independent of the specific pulse duration and wavelength.

We have observed quite similar properties also in the case of laser ablation of metallic targets irradiated in similar conditions as for silicon [11]. As an example, Fig. 7 reports the size distribution of the nanoparticles produced during laser ablation of a nickel target with 0.9 ps/1055 nm and 0.1 ps/780 nm, at a

Table 1
Statistical parameters of the fit of a lognormal distribution to the experimental size distributions of silicon nanoparticles produced with the two laser pulses used in the present work, at three different values of the laser intensity I_L

Laser, τ_L (ps)/ λ (nm)	I_L (W/cm ²)	r_c (nm)	w	r_{peak} (nm)	r_- (nm)	r_+ (nm)
0.9 ps/1055 nm	3.3×10^{11}	4.2	0.6	2.9	2.3	7.7
	5.0×10^{11}	7.4	0.8	3.9	3.3	16.5
	6.7×10^{11}	12.1	0.4	10.3	8.1	18.1
0.1 ps/780 nm	3.0×10^{12}	6.1	0.7	3.7	3.0	12.3
	6.0×10^{12}	8.3	0.7	5.1	4.1	16.7
	1.1×10^{13}	8.0	0.7	4.9	4.0	16.1

r_c is the median radius and w is the standard deviation of the logarithmic of the radius. r_{peak} is the most probable radius, while r_- and r_+ represent the nanoparticles radius below and above which 16% of the nanoparticles are counted, i.e. 68% of the nanoparticles have a radius lying between r_- and r_+ .

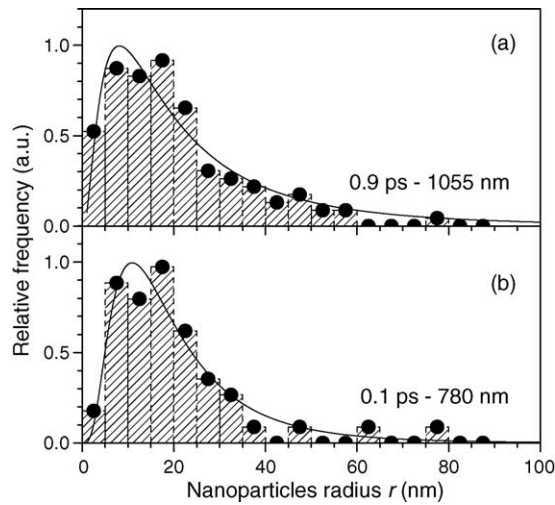


Fig. 7. Size distribution of the nickel nanoparticles produced during laser ablation with the two laser pulses used in the present work: (a) 0.9 ps/1055 nm laser pulses at a laser intensity of 3.3×10^{11} W/cm²; (b) 0.1 ps/780 nm laser pulser at a laser intensity of 3×10^{12} W/cm². The solid curve represents the fit to a log-normal distribution.

Table 2
As in Table 1 for nickel sample

Laser, τ_L (ps)/ λ (nm)	I_L (W/cm ²)	r_c (nm)	w	r_{peak} (nm)	r_- (nm)	r_+ (nm)
0.9 ps/1055 nm	3.3×10^{11}	18.4	0.9	8.2	7.5	45.3
	6.7×10^{11}	20.5	0.5	16.0	12.4	33.8
	8.9×10^{11}	27.3	0.4	23.3	18.3	40.7
0.1 ps/780 nm	3.0×10^{12}	17.0	0.7	10.4	8.4	34.2
	6.0×10^{12}	15.0	0.7	9.2	7.4	30.2
	1.1×10^{13}	20.4	1.0	7.5	7.5	55.5

laser intensity of 3.3×10^{11} and 3.0×10^{12} W/cm², respectively. The size statistics of the nickel nanoparticles at three different laser intensities are summarized in Table 2. We observe nickel nanoparticles with radii ranging from few nm to ≈ 50 nm, with a median radius of the order of 15–25 nm and a peak radius smaller than ≈ 15 nm. As for silicon, the size histogram is fairly well described by a lognormal distribution. Moreover, also for nickel 84% of the nanoparticles show a radius below ≈ 40 nm, independently of laser intensity and pulse length, and both r_c and r_{peak} only slightly increase with the laser intensity.

6. Discussion and conclusions

We have analyzed the properties of the material blow-off produced during laser irradiation of solid targets with laser pulses of different durations at near-infrared wavelengths, namely 0.9 ps/1055 nm and 0.1 ps/780 nm. Our experimental results on infrared laser ablation process at two different laser pulse durations evidence that the material blow-off induced by ultrafast laser heating followed by vacuum expansion is characterized by some general features, whichever the nature of the target material, silicon or nickel e.g. In particular, laser

ablation of solid targets inevitably leads to the generation of an ablation plume composed of a fast plume component formed by atoms and ions of the target material, which expands at typical velocities of $\approx 10^6$ cm/s or larger, which is followed by a much slower component of nanoparticles of the target material, characterized by a centre-of-mass expansion velocity along the normal to the target surface of the order of 10^4 cm/s. This difference in the velocity distribution suggests that the nanoparticles are not formed through condensation processes in the dilute atomic vapor formed during vacuum expansion; rather they are predominantly produced in the relaxation of the extreme material state created by the intense, ultrashort laser pulse, in agreement with current models of ultrashort laser ablation. In this respect, it is worth to notice that for nickel, the linear absorption coefficient α_0 is of the order of $(6-8) \times 10^5$ cm⁻¹, at the two infrared wavelengths considered here [36], resulting in a skin depth of $\alpha_0^{-1} \approx 14$ nm. On the other hand, in silicon the laser light is mainly absorbed via avalanche ionization, as discussed in Section 4, with the formation of a high electron density plasma in a thin layer with a thickness of hundreds of nanometers. The subsequent thermophysical response of the underlying material occurs through plasma heating and/or ultrafast phase transformation to a metallic state.

Thus, for both materials the laser energy is absorbed in a thin surface layer and delivered to matter in so short a timescale (≤ 1 ps) that absorption and heating occur at nearly solid-state density (near isochoric heating). Therefore, the heated layer reaches very high temperatures, which are accompanied by the buildup of strong pressure gradients within the material. A nearly adiabatic expansion of the heated material eventually occurs, with a consequent decrease of density and temperature. It is during this adiabatic cooling that parts of the system can be driven into a metastable region of the phase diagram, resulting in the production of a relatively large fraction of nanoparticles via different mechanisms as suggested in recent numerical analysis of femtosecond laser ablation of solid targets under different heating regimes. In particular, for the systems considered in the present work, it has been suggested that photomechanical effects can play an important role in the material removal process [37,38]. Photomechanical effects becomes significant when both the laser pulse duration, τ_p , and the time of energy transfer from the electronic subsystem to the lattice, τ_{e-l} , are shorter than the time needed for the mechanical equilibration of the absorbing volume, τ_s (inertial or stress confinement): $\tau_p, \tau_{e-l} \leq \tau_s$. The time needed for the relaxation of the thermoelastic stress can be estimated as: $\tau_s \approx \frac{L_p}{c_s}$, where L_p and c_s are the characteristic depth of laser energy deposition and the speed of sound in the material, respectively. For silicon $\tau_{e-l} \approx 1$ ps, $L_p \approx 100-400$ nm, and $c_s \approx 2$ nm/ps [36], leading to $\tau_s \approx 50-200$ ps. For nickel $\tau_{e-l} \approx 5$ ps [37], $L_p \approx 50-100$ nm [38] and $c_s \approx 5$ nm/ps [36], giving $\tau_s \approx 10-20$ ps. Therefore, in our experimental conditions we are in a stress confinement regime for both laser pulse durations. This makes very likely that the observed nanoparticles are formed during the relaxation of the critical state of the material induced by ultrashort laser irradiation through photomechanical effects.

References

- [1] B. Rethfeld, K. Sokolowski-Tinten, D. von der Linde, S.I. Anisimov, *Appl. Phys. A* 79 (2004) 767.
- [2] L.V. Zhigilei, *Appl. Phys. A* 76 (2003) 339.
- [3] D. Bäuerle, *Laser Processing and Chemistry*, 3rd ed., Springer, Berlin, 2000.
- [4] B.B. Chrisey, G.K. Hubler (Eds.), *Pulsed Laser Deposition of Thin Films*, John Wiley and Sons, New York, 1994.
- [5] L. Jiang, H.L. Tsai, in: *Proceedings of NSF Workshop on Research Needs in Thermal Aspects of Material Removal*, Stillwater, OK, 2003, p. 163.
- [6] S. Nolte, C. Momma, H. Jacobs, A. Tünnermann, B.N. Chichkov, B. Wellegehausen, H. Welling, *J. Opt. Soc. Am. B* 14 (1997) 2716.
- [7] M. Lenzner, J. Kruger, S. Sartania, Z. Cheng, C. Spielmann, G. Mourou, W. Kautek, F. Krausz, *Phys. Rev. Lett.* 80 (1998) 4076.
- [8] N.N. Nedialkov, S.E. Imamova, P.A. Atanasov, *J. Phys. D: Appl. Phys.* 37 (2004) 638.
- [9] L. Jiang, H.L. Tsai, *J. Phys. D: Appl. Phys.* 37 (2004) 1492.
- [10] S. Amoruso, R. Bruzzese, N. Spinelli, R. Velotta, M. Vitiello, X. Wang, G. Ausanio, V. Iannotti, L. Lanotte, *Appl. Phys. Lett.* 84 (2004) 4502.
- [11] S. Amoruso, G. Ausanio, R. Bruzzese, M. Vitiello, X. Wang, *Phys. Rev. B* 71 (2005) 033406.
- [12] S. Amoruso, C. Altucci, R. Bruzzese, C. De Lisio, N. Spinelli, R. Velotta, M. Vitiello, X. Wang, *Appl. Phys. A* 79 (2004) 1377.
- [13] J.R. Goldman, J.A. Prybyla, *Phys. Rev. Lett.* 72 (1994) 1364.
- [14] S. Amoruso, R. Bruzzese, N. Spinelli, R. Velotta, M. Vitiello, X. Wang, *Europhys. Lett.* 67 (2004) 404.
- [15] F. Qian, V. Craciun, R.K. Singh, S.D. Dutta, P.P. Pronko, *J. Appl. Phys.* 86 (1991) 2281.
- [16] S. Amoruso, X. Wang, C. Altucci, C. de Lisio, M. Armenante, R. Bruzzese, R. Velotta, *Appl. Phys. Lett.* 77 (2000) 3728.
- [17] M. Ye, C.P. Grigoropoulos, *J. Appl. Phys.* 89 (2001) 5183.
- [18] O. Albert, S. Roger, Y. Glinec, J.C. Loulergue, J. Etcheparre, C. Boulmer-Lborgne, J. Perrière, E. Millon, *Appl. Phys. A* 76 (2003) 319.
- [19] N.M. Bulgakova, R. Stoian, A. Rosenfeld, I.V. Hertel, E.E.B. Campbell, *Phys. Rev. B* 69 (2004) 054102.
- [20] R. Stoian, A. Rosenfeld, D. Ashkenasi, I.V. Hertel, N.M. Bulga-kova, E.E.B. Campbell, *Phys. Rev. Lett.* 88 (2002) 097603.
- [21] W.G. Roeterdink, L.B.F. Juurlink, O.P.H. Vaughan, J. Dura-Diez, M. Bonn, A.W. Kleyn, *Appl. Phys. Lett.* 82 (2003) 4190.
- [22] R.F.W. Herrmann, J. Gerlach, E.E.B. Campbell, *Nucl. Instrum. Meth. Phys. Res. B* 122 (1997) 401.
- [23] S.I. Kudryashov, V.I. Emel'yanov, *JEPT Lett.* 73 (2001) 666.
- [24] A.V. Bulgakov, I. Ozerov, W. Marine, *Appl. Phys. A* 79 (2004) 1591.
- [25] E.G. Gamaly, A.V. Rode, B. Luther-Davies, V.T. Tikhonchuk, *Phys. Plasmas* 9 (2002) 949.
- [26] Z. Zhang, P.A. Van Rompay, J.A. Nees, C.A. Stewart, X.P. Pan, L. Fu, P.P. Pronko, *Proc. SPIE* 3935 (2000) 86.
- [27] S. Amoruso, X. Wang, C. Altucci, C. de Lisio, M. Armenante, R. Bruzzese, N. Spinelli, R. Velotta, *Appl. Surf. Sci.* 186 (2002) 358.
- [28] B.C. Stuart, M.D. Feit, S. Hermann, A.M. Rubenchik, B.W. Shore, M.D. Perry, *Phys. Rev. B* 53 (1996) 1749.
- [29] P.P. Pronko, S.K. Dutta, J. Squier, J.V. Rudd, D. Du, G. Mourou, *Opt. Commun.* 114 (1995) 106.
- [30] P.P. Pronko, P.A. Van Rompay, C. Horvath, F. Loesel, T. Juhasz, X. Liu, G. Mourou, *Phys. Rev. B* 58 (1998) 2387.
- [31] D.H. Reitze, T.R. Zhang, Wm.M. Wood, M.C. Downer, *J. Opt. Soc. Am. B* 7 (1990) 84.
- [32] K.K. Thornber, *J. Appl. Phys.* 52 (1981) 279.
- [33] E. Yablonovich, N. Bloembergen, *Phys. Rev. Lett.* 29 (1972) 907.
- [34] K. Sokolowski-Tinten, D. von der Linde, *Phys. Rev. B* 61 (2000) 2643.
- [35] P.L. Silvestrelli, A. Alavi, M. Parinello, D. Frenkel, *Phys. Rev. B* 56 (1997) 3806.
- [36] D.R. Lide, *CRC Handbook of Chemistry and Physics*, 75th ed., CRC Press, Boca Raton, 1994.
- [37] D.S. Ivanov, L.V. Zhigilei, *Phys. Rev. B* 68 (2003) 064114.
- [38] D.S. Ivanov, L.V. Zhigilei, *Appl. Phys. A* 79 (2004) 977.